Axisymmetric models for neutron star merger remnants with realistic thermal and rotational profiles

Giovanni Camelio,[1,2] Tim Dietrich,[3] Stephan Rosswog,[2] and Brynmor Haskell[1]

[1]*Nicolaus Copernicus Astronomical Center, Polish Academy of Science, Bartycka 18, 00-716 Warsaw, Poland*

[2]*Astronomy and Oskar Klein Centre, Stockholm University, AlbaNova, SE-10691 Stockholm, Sweden*

[3]*Institute of Physics and Astronomy, University of Potsdam, 14476 Potsdam, Germany*

(Received 20 November 2020; accepted 15 February 2021; published 11 March 2021)

Merging neutron stars are expected to produce hot, metastable remnants in rapid differential rotation, which subsequently cool and evolve into rigidly rotating neutron stars or collapse to black holes. Studying this metastable phase and its further evolution is essential for the prediction and interpretation of the electromagnetic, neutrino, and gravitational signals from such a merger. In this work, we model binary neutron star merger remnants and propose new rotation and thermal laws that describe postmerger remnants. Our framework is capable to reproduce quasiequilibrium configurations for generic equations of state, rotation and temperature profiles, including nonbarotropic ones. We demonstrate that our results are in agreement with numerical relativity simulations concerning bulk remnant properties like the mass, angular momentum, and the formation of a massive accretion disk. Because of the low computational cost for our axisymmetric code compared to full $3+1$-dimensional simulations, we can perform an extensive exploration of the binary neutron star remnant parameter space studying several hundred thousand configurations for different equations of state.

DOI: 10.1103/PhysRevD.103.063014

I. INTRODUCTION

With densities substantially exceeding those in atomic nuclei, neutron stars (NSs) provide an interesting "astrophysical laboratory" to probe matter under the most extreme conditions and they can deliver physical information that complements other ongoing efforts to understand nuclear matter [1,2]. NSs originate in supernova explosions or binary neutron star (BNS) mergers [3]. In either case, they are hot and differentially rotating in the first minute of their lives [4,5]. Because of the growing possibilities of detecting them via gravitational wave interferometers and in the whole electromagnetic spectrum (from radio to gamma rays [6]), and because they involve nuclear matter at densities and temperatures that cannot be probed in terrestrial experiments, BNS remnants have been carefully investigated in a number of recent studies, e.g., [7–12].

The physical realism of $3+1$ numerical relativity simulations has enormously increased over recent years, but realistic simulations come at the price of several hundred thousand core hours on supercomputers per physical millisecond, which makes an efficient exploration of the remnant parameters impossible. Moreover, studies that focus on the exploration of the microphysics, such as the effects of neutrino oscillations [13–15], need physically motivated background models but usually cannot afford at the same time a $3+1$ numerical relativity approach. For these reasons very fast, yet still physically reliable, axisymmetric models of newly formed merger remnants are needed.

The vast majority of NS studies neglect differential rotation and assume rigid rotation. The first model of a NS in differential rotation made use of the so-called j-constant rotation law[1] [16,17], which is a good qualitative description of the protoneutron star formed in a core-collapse supernova, where the core rotates faster than the envelope. In order to improve on these approximations, Uryū *et al.* [18] proposed a new model for the rotation profile of a BNS merger remnant that mimics the output of dynamical simulations [5,19–21], where the angular velocity reaches a maximum in the envelope and approaches Keplerian rotation at large radii. Since then, other authors used Uryū and collaborators' model [22–24]. However, a proper inclusion of the thermal profile of the BNS merger

[1]Note that with this differential rotation law the specific angular momentum is not constant in general, but only in a particular limit and in Newtonian gravity.

remnant, which can reach temperatures up to a hundred MeV, has not been done yet. Moreover, until recently, hot NS models had been obtained through the so-called effectively barotropic approximation, where all thermodynamical quantities were put in a one-to-one relation [25]. This is a strong assumption for a remnant that is expected to be baroclinic, i.e., not effectively barotropic [4]. Recently, Camelio *et al.* [26] developed a technique to obtain a stationary, hot, differentially rotating, baroclinic NS model, opening the way to a larger class of thermal and rotational profiles.

Modeling BNS merger remnants with stationary codes is an important complementary approach to full hydrodynamical simulations, since it allows for a much faster and wider exploration of the possible parameter space. In addition, stationary configurations can be used as initial profiles for dynamical simulations. Last but not least, the study of stationary configurations provides important indications on stellar stability [25,27–32]. This is important because unstable stars are more likely to be observed through gravitational, neutrino, and electrodynamic radiation, e.g., [3,6,33,34], allowing for an in-depth study of the involved physics.

In this work, we first develop a model for the stationary remnant of a BNS system at ∼10–50 ms after merger, which is differentially rotating, hot, and baroclinic (Sec. II). In particular, we propose new rotation and thermal laws for the remnant and apply the baroclinic formalism developed by Camelio *et al.* [26]. We then explore the model parameter space and discuss the remnant stability with simple heuristics (Sec. III). We conclude in Sec. IV. In the Appendix, we provide details of our numerical implementation. The parameter space exploration results and the profiles of the most realistic stellar models found are available to the community on Zenodo [35].

Unless otherwise specified, we set $c = G = M_\odot = k_B = 1$. Our code unit for lengths approximately corresponds to 1.477 km, that for angular velocity to 32.31 kHz 2π rad, that for energy to 1.115×10^{60} MeV, and that for time to 4.925 μs. Moreover, the saturation density is $\rho_n = 4.339 \times 10^{-4}$ and the neutron mass is $m_n = 8.423 \times 10^{-58}$.

II. MODEL

A. Equation of state

The equations of state (EOSs) adopted in this work are piecewise polytropes with a crust [36] and a thermal component [26]:

$$\epsilon(\rho, s) = (1 + a_i)\rho + k_i\rho^{\Gamma_i} + k_{\rm th}s^2\rho^{\Gamma_{\rm th}}, \tag{1}$$

where ϵ, ρ, s are respectively the total energy density, the rest mass density, and the entropy per baryon, a_i, k_i, Γ_i are cold piecewise polytropic parameters valid in a given density range $\rho_{i-1} < \rho < \rho_i$ and are obtained by fits [36], $\Gamma_{\rm th} = 1.75$ is the thermal exponent and we set its value so that it is in the range expected for the high-density part of the EOS [37,38], and $k_{\rm th}$ is the thermal constant and its value is determined for each EOS so that the thermal pressure at $\rho = 2\rho_n$ and $s = 2\ {\rm k_B}$ is 30% of the cold pressure. This value has been chosen after inspecting tabulated EOSs and could be easily adjusted for further studies, if needed. We consider a subset of EOSs from Read *et al.* [36] that fulfill the most recent radius and maximum mass constraints obtained from nuclear physics and astrophysical observations [39]: ALF2 [40], SLy [41], APR4 [42], and ENG [43], see Appendix A 1.

B. Euler equation

We determine the NS configuration with our version [26,32] of the eXtended conformal flatness Neutron Star (XNS) code [44,45]. The code assumes stationarity (and hence axisymmetry), circularity (and hence the absence of meridional currents), and conformal flatness [46,47]. The conformal flatness assumption does not change the theory of the modeling of the neutron star and its stability described in this section; however, the exact values of the total stellar quantities like mass and angular momentum may vary at most up to a few percent with respect to the values obtained in full general relativity [24,48]. This level of precision is acceptable for this initial study.

It is possible [26] to cast the Euler equation in a form that is reminiscent of thermodynamical equations,

$$\mathrm{d}Q(p, F) = \frac{\mathrm{d}_p}{\hbar} - \Omega \mathrm{d}F, \tag{2}$$

by defining the potential

$$Q(p, F) = -\ln\frac{\alpha(r, \theta)}{\Gamma(r, \theta, F)} - \Omega(r, \theta, F)F, \tag{3}$$

where p is the pressure, $\hbar = \epsilon + p$ the total enthalpy density, r, θ are respectively the quasi-isotropic radius and polar angle coordinates, $\Omega = u^\phi/u^t$ is the fluid angular velocity seen from infinity (u is the fluid four-velocity), $F = u^t u_\phi$ is the redshifted angular momentum per unit enthalpy and unit rest mass [24], α is the lapse function, and $\Gamma = \alpha u^t$ is the Lorentz factor with respect to the zero angular momentum observer. From Eqs. (2) and (3) it follows that the angular velocity Ω and the enthalpy density $\hbar$ can be obtained by differentiation:

$$\Omega = -\left.\frac{\partial Q(p, F)}{\partial F}\right|_p, \tag{4}$$

$$\frac{1}{\hbar} = \left.\frac{\partial Q(p, F)}{\partial p}\right|_F. \tag{5}$$

The advantage of using the potential Q to define the stellar model is that in this way we can obtain "baroclinic"

configurations [26] that allow for a more realistic representation of merger remnants [4] than the commonly used "effectively barotropic" approximation. In an effectively barotropic model, one thermodynamical variable fixes all the other ones, while this is not true in a baroclinic model. Note that we choose a version of the potential Q that depends on F instead of Ω since in a BNS merger remnant the profile of the angular velocity is not monotonic [18,21,26].

Our model for a BNS merger remnant is defined by the following potential:

$$Q(p,F) = H(p) + G(F) + bH(p)G(F), \tag{6}$$

$$H(p) = \int_{\rho_0}^{\tilde{\rho}(p)} \frac{p'}{\hbar(\tilde{\rho},\tilde{s}(\tilde{\rho}))}\mathrm{d}\tilde{\rho}, \tag{7}$$

where b is the baroclinic parameter, $H(p)$ is the "heat function," $G(F)$ is the "rotation law,"[2] ρ_0 is a parameter equivalent to the central density,[3] $\tilde{s}(\rho)$ is (one version of) the "thermal law," namely a one-to-one relationship between the thermodynamical quantities, and p' and $\rho(p)$ the total derivative of $\tilde{p}(\rho) = p(\rho,\tilde{s}(\rho))$ and its inverse, respectively. To solve the Euler equation in a point, one has to solve Eqs. (3) and (4) in order to obtain the pressure p and angular velocity Ω in that point, get the enthalpy density $\hbar$ from Eq. (5), and then (optionally) invert the EOS to obtain the other thermodynamical quantities ρ, s, T. The quantities $\tilde{s},\tilde{\rho},\tilde{\hbar} = \hbar(\tilde{\rho},\tilde{s}(\tilde{\rho}))$ that appear in Eq. (7) are equivalent to the physical thermodynamical quantities s, ρ, $\hbar$ only when the star is effectively barotropic (i.e., $b = 0$), in which case $\hbar$ depends only on the pressure p and the angular speed Ω depends only on F [cf. Eqs. (4) and (5)] [49].

To complete the definition of our model, we must choose the rotation and thermal laws. For the rotation law, we propose

$$G(F) = \begin{cases} F < F_0: & G_0 - \Omega_0 F - (\Omega_M - \Omega_0)F \cdot \left(\left(\frac{F}{F_0}\right)^2 - \frac{1}{2}\left(\frac{F}{F_0}\right)^3\right) \\ F > F_0: & G_0 - \frac{\Omega_0+\Omega_M}{2}F_0 + \frac{\Omega_M}{\sigma}\left(\frac{1+2\sigma(F-F_0)}{(1+\sigma(F-F_0))^3} - 1\right), \end{cases} \tag{8}$$

where $G_0\Omega_0$, Ω_M, F_0, and σ are free parameters. This rotation law is smooth (its second derivative is continuous), it has an easy analytical form, a minimum (respectively maximum) at the center (respectively at F_0), and it is Keplerian at large radii.[4] When the star is effectively barotropic ($b = 0$), the derivative $\tilde{\Omega} = -G'(F)$ is equal to the angular velocity profile, see Fig. 1(a) and cf. Eqs. (4) and (6). In this case, Ω_0 and Ω_M are the axial and maximum angular velocities, the latter reached of axis exactly at F_0. F_0 (respectively σ^{-1}) is the scale of the variation for the low (respectively high) angular momentum part of the rotation law. To reduce the number of free parameters, we assume that $G_0 = 0$, which implies that ρ_0 and Ω_0 are the central density and axial angular velocity[5] also in the baroclinic case [26], and that G''' is continuous in F_0, which leads to

$$F_0 = \sqrt{\frac{\Omega_M - \Omega_0}{2\Omega_M}}\sigma^{-1}. \tag{9}$$

During the first tens of milliseconds after the merger, the remnant is not isentropic [4]: temperature and entropy increase for decreasing density up to a critical value where the temperature peaks. At lower densities the temperature decreases adiabatically, while the entropy per baryon keeps increasing, but with a lower rate. This behavior can be reproduced with our EOS assuming the following thermal law [see Figs. 1(b) and 1(c)]:

$$\tilde{s}(\rho) = k_s \frac{\rho^{1-\Gamma_{\mathrm{th}}+\Gamma_T}}{1+\exp(\frac{\rho-\rho_M}{\rho_L})}, \tag{10}$$

with $\Gamma_{\mathrm{th}} - 1 > \Gamma_T > 0$, which implies

$$\tilde{T}(\rho) = 2m_n k_{\mathrm{th}} k_s \frac{\rho^{\Gamma_T}}{1+\exp(\frac{\rho-\rho_M}{\rho_L})}, \tag{11}$$

where ρ_M is approximately the peak density for the temperature and ρ_L is a density scale, k_s is a multiplicative constant that sets the scale of the entropy, and Γ_T is the temperature polytropic index at lower density. Following the description of Perego *et al.* [4] of the BNS merger remnant at ∼10 ms after the merger, we set $\rho_m = \rho_L = \rho_n$

[2]Note that Uryū *et al.* [18] call rotation law the quantity $-G'$, which in the nonbarotropic case they consider ($b = 0$) is equivalent to the angular velocity Ω.

[3]This is true if $b = 0$ or $G(0) = 0$, as done in this paper.

[4]That is, $\Omega \propto F^{-3}$ as $r \to \infty$. Note however that, in general, it is not guaranteed that it reaches Keplerian frequency at large radii. This is true also for the rotation law of Uryū *et al.* [see Eq. (8) of [18]].

[5]Note that $G_0 \neq 0$ would be necessary to reproduce shellular rotation, which however is not relevant for the BNS merger remnant.

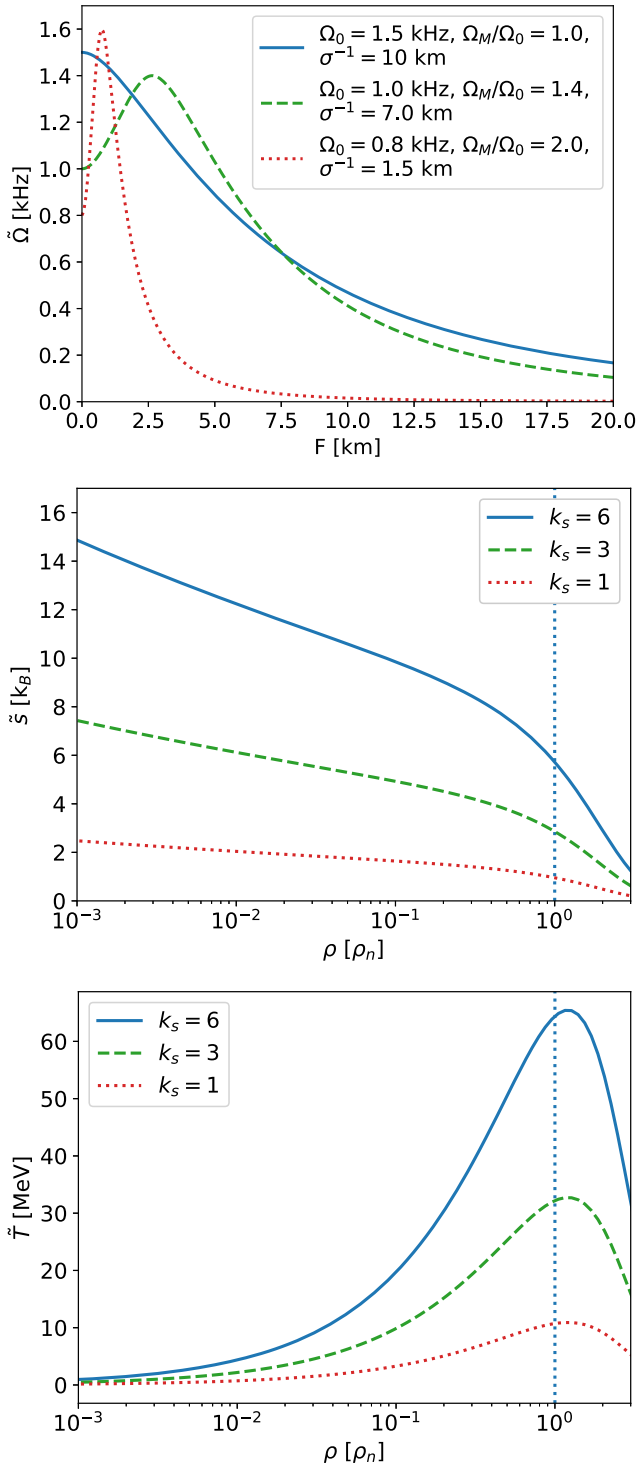

FIG. 1. Dependence on the parameters of the rotation and thermal laws. $\tilde{\Omega} = -G'(F)$ (top) is minus the derivative of the rotation law and $\tilde{s}$ (center) and $\tilde{T}$ (bottom) are two equivalent versions of the thermal law. If the star is effectively barotropic ($b = 0$), then $\Omega = \tilde{\Omega}$, $s = \tilde{s}$, $T = \tilde{T}$. The vertical blue dotted line marks the saturation density.

and $\Gamma_T = 2/3$ (i.e., adiabatic expansion in the envelope). At later times (20–30 ms) and in the low-density region $\rho < 10^{-4}\rho_n$, this value is expected to decrease to $\Gamma_T = 1/3$ [4].

III. RESULTS

A. Search

For each EOS, we run about 100,000 simulations in order to explore the parameter space, varying the following six parameters with a uniform distribution:

(i) central density $\rho_0 = [2; 10]\rho_n$,
(ii) axial angular velocity $\Omega_0 = [0; 3]$ kHz,
(iii) entropy scale $k_s = [1; 9]$,
(iv) maximal-to-axial angular velocity ratio $\Omega_M/\Omega_0 = [1; 2]$,
(v) rotation law scale $\sigma^{-1} = [1.5, 10]$ km (we report it in km because it can be interpreted, approximately, as the radial scale of the rotation distribution at large distance from the rotation axis),
(vi) baroclinic constant $b = [-2; 0]$.

As already discussed, see Sec. II B, the other parameters are set as follows: $G_0 = 0$, F_0 from Eq. (9), $\rho_M = \rho_L = \rho_n$, and $\Gamma_T = 2/3$. The values and ranges of the parameters are chosen to approximately reproduce the models evolved by Hanauske *et al.* [5] and Perego *et al.* [4] (see Sec. III D for a comparison). In particular, we set $b < 0$ so that there is a hot ring in the equatorial plane instead of two hot caps in the polar regions and its range is set to resemble the models of Perego *et al.* [4] and Kastaun *et al.* [21], and to include the effectively barotropic model as special case ($b \to 0$). The numerical details of how we find our solutions with a modified version of the XNS code are reported in Appendix A 2.

We remark that time evolution of the BNS remnant can be mimicked by varying the free input parameters of our model, once the remnant becomes stationary after a $\sim$10 ms timescale. In fact, shortly after merger, $b \to 0$ on a $t \simeq 50$ ms timescale [4] and at later times, if the remnant does not collapse to a black hole, $k_s \to 0$ on a $t \simeq 10$ s timescale due to the loss of entropy caused by neutrino emission. On this timescale the central density ρ_0 increases due to cooling and $\Omega_M/\Omega_0 \to 1$ and $\sigma \to 0$ as the star approaches rigid rotation due to neutrino diffusion and magnetic viscosity (both of which we do not include). Whether the axial angular velocity Ω_0 increases or decreases on a longer timescale depends on the total angular momentum loss by neutrino emission and magnetic braking [33,34], on that gained by accretion, and by the evolution of the stellar moment of inertia. However, it is plausible to assume that the BNS merger remnant spins up as it happens for a protoneutron star [50].

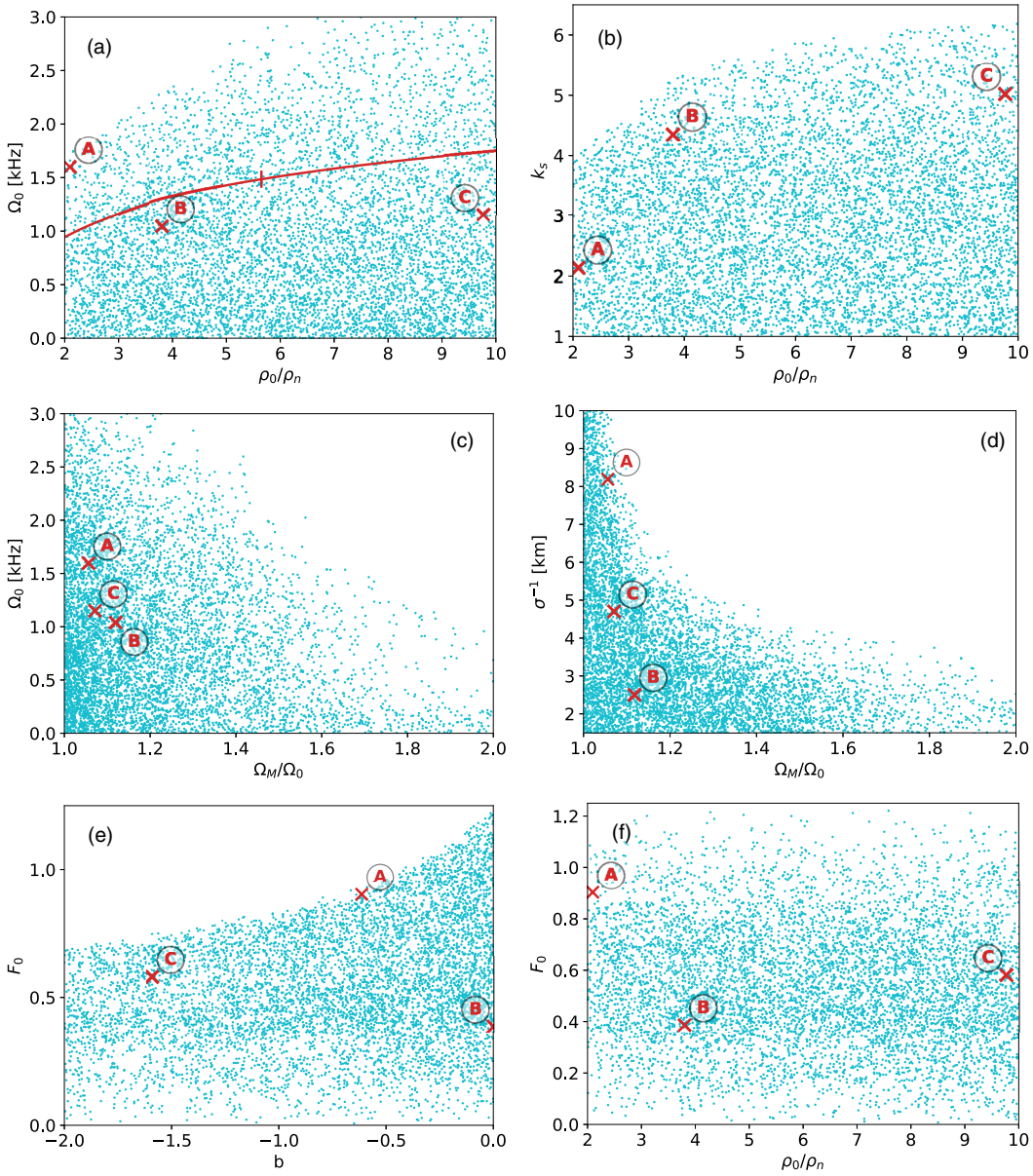

FIG. 2. Parameter space of the BNS merger remnant with the ALF2 EOS. The blue dots are the successful runs with $M < 4$ and the red line is the rigidly rotating, cold Keplerian curve, on which we marked the marginally stable configuration. We marked with red crosses the model described in Sec. III D. ρ_0 is the central density, Ω_0 the angular velocity on the rotational axis, k_s the entropy scale, Ω_M/Ω_0 the ratio between the maximum and axial angular velocity in the rotation law, σ^{-1} the rotation law scale, F_0 the critical point of the rotation law, and b the baroclinic parameter.

Before discussing the results, we remark that only ~7%–8% of the parameter combinations in the searches gives a valid solution of the Einstein and Euler equations. The failure of a particular parameter combination may be due to the physics (e.g., the mass shedding limit has been exceeded) or to numerical issues (i.e., the code is not stable enough; a "false negative"). We increased the stability of the code by choosing physically motivated parameters and by slowly increasing the rotational and thermal content of the star at the beginning of the iterative process (see Appendix A 2). However, it is unavoidable that a fraction of the unsuccessful runs might consist of false negatives. On the other hand, the successful configurations are physical in the sense that they are solutions of the Einstein and Euler equations, but despite our efforts of realistic modeling we cannot be sure that they all approximate the result of dynamical evolution of mergers. For example, a small number of successful parameter combinations (of the order 10) results in stellar models with gravitational mass $M > 4$. Considering BNS population scenarios, such high masses are astrophysically unlikely (but not impossible for rapidly rotating models with

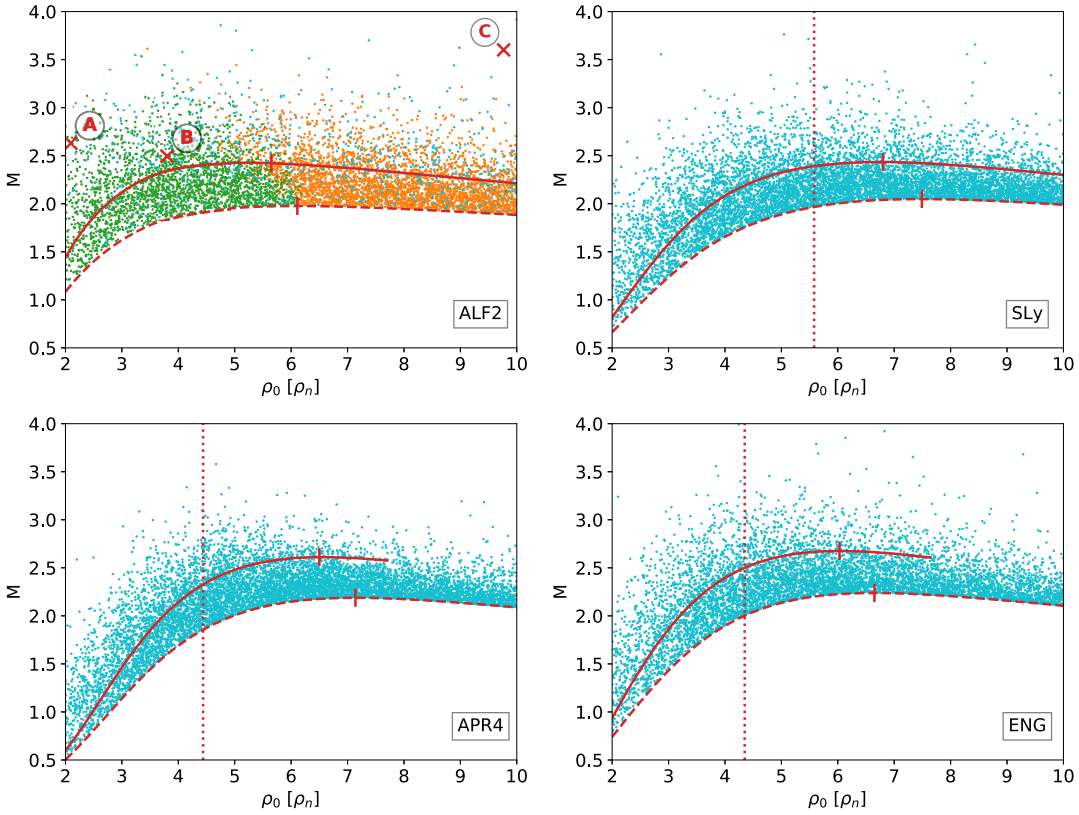

FIG. 3. Mass M vs central density ρ_0 for each EOS. Plotting conventions are as in Fig. 2; in addition the red dashed line is the nonrotating curve on which we marked the maximal mass configuration and the vertical dotted line is the critical density ρ_c for the EOS inversion, see Appendix A 1. For the ALF2 EOS, we colored each point according to criterion (16): green and orange points are expected to be stable and unstable, respectively, while we do not known the value of Eq. (16) for blue points (due to numerical issues). We stress that this stability criterion [Eq. (16)] *cannot* be applied to our model and we report it here only as an *indication*, see discussion in Sec. III C for details.

extremely stiff EOSs [51]) for BNS merger remnants and we will exclude these configurations from the following analysis.

Unless otherwise stated, we will consider the ALF2 EOS in this section. The reason is that we can reliably invert the EOS and obtain the rest mass density ρ and entropy per baryon s from the pressure p and the enthalpy density $\hbar$ only for this EOS (see Appendix A 1 for details). We checked that the other quantities follow the same qualitative trends of the ALF2 EOS, see for example Fig. 3.

The parameters and stellar quantities of the successful configurations found in the search can be downloaded from Zenodo [35].

B. Stellar properties

By exploring several thousand configurations, we find that some combinations of the model parameters are either unphysical or not reproducible with our code, see Fig. 2 and discussion in Sec. III A. In some cases, there is a reasonable physical motivation for trends observed in Fig. 2: for example, the maximum of the axial angular velocity Ω_0 increases with density ρ_0 [Fig. 2(a)], since gravity is stronger and it is possible to reach faster rotation without mass shedding, cf. Fig. 4(b). Similarly, the maximum of the entropy scale k_s increases with increasing density ρ_0 [Fig. 2(b); the other EOSs reach $k_s = 9$ with a similar trend of ALF2] and the maximum of the axial angular velocity Ω_0 is greater for smaller rotation ratio Ω_M/Ω_0 [Fig. 2(c)], due to the necessity for the equatorial angular velocity to be lower than the Keplerian frequency in order to avoid mass shedding. On the other hand, the fact that the maximum of the rotation scale σ^{-1} is greater for smaller rotation ratio Ω_M/Ω_0 is probably a spurious effect due to numerical issues, since in simulations [5] the distance of the maximum of the angular velocity profile is at larger distances from the rotational axis than what we obtain with our code, see Figs. 2(d) and 8 and discussion in Sec. III D. Remarkably, the position of the maximum of the angular velocity F_0 (which also serves as a scale for the inner part of the rotation law) is correlated with the baroclinic constant b, while it is not correlated with the central density ρ_0 [Figs. 2(e) and 2(f)] and with k_s.

For a given central density, the gravitational mass M of our BNS merger remnant model is larger than the

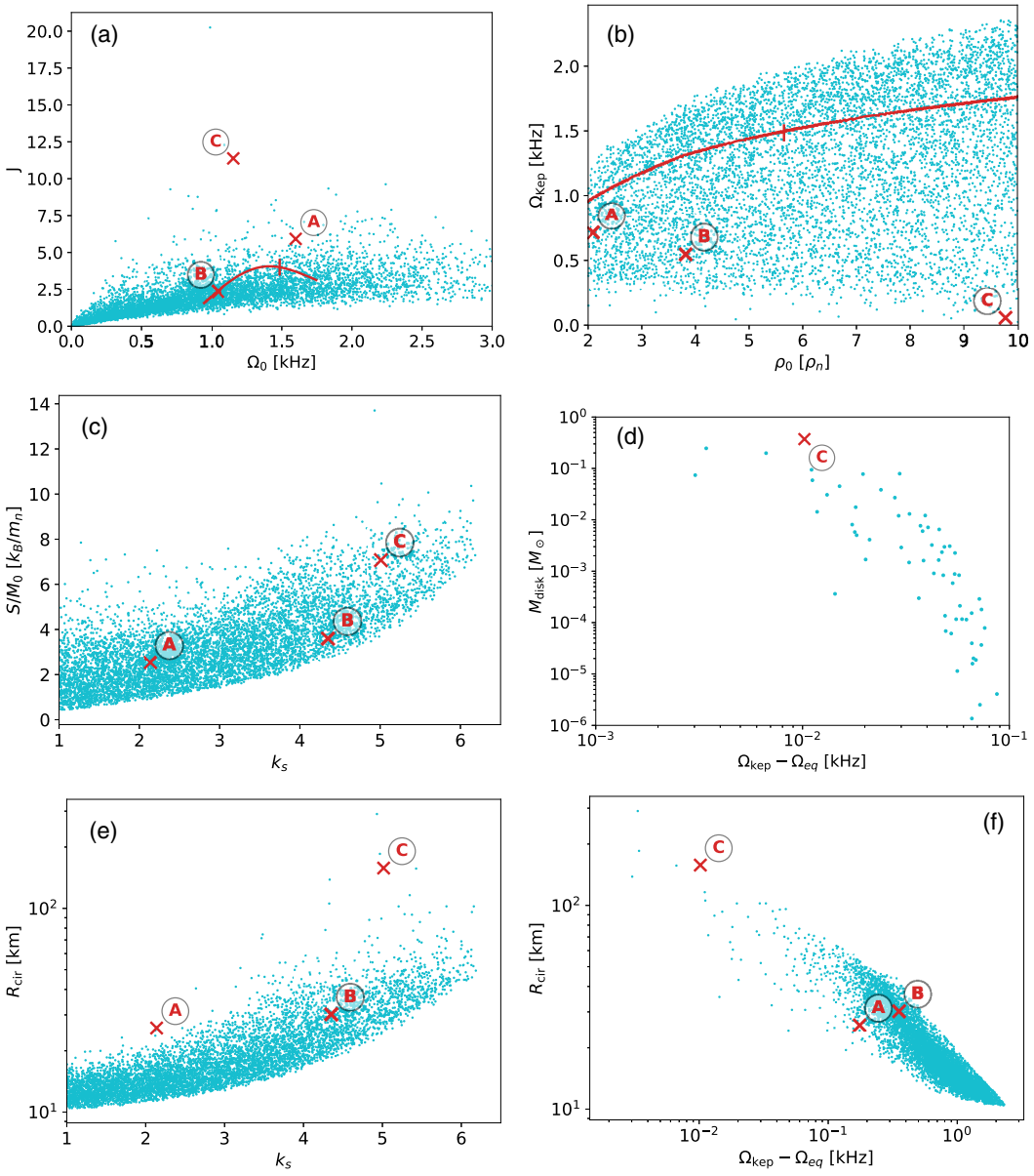

FIG. 4. Stellar properties of the BNS merger remnant with the ALF2 EOS. Plotting conventions are as in Fig. 2. Ω_0 is the angular velocity on the rotational axis, J the angular momentum, ρ_0 the central density, $\Omega_{\rm kep}$ the Keplerian angular velocity at the equator, k_s the entropy scale parameter, S/M_0 the average (per baryon mass) stellar entropy, $\Omega_{\rm eq}$ the angular velocity at the equator, $M_{\rm disk}$ the expected baryon mass of the accretion disk, and $R_{\rm cir}$ the circumferential equatorial radius.

nonrotating mass and can even be larger than the cold rigidly rotating Keplerian one, see Fig. 3. In Fig. 4 we show some trends of other stellar quantities. These trends are obvious and expected: the stellar angular momentum J grows with the axial angular velocity Ω_0 [Fig. 4(a)], the maximum of the Keplerian angular velocity $\Omega_{\rm kep}$ grows with the central density ρ_0, and the average entropy per baryon S/M_0 grows with the entropy scale k_s. The circumferential radius $R_{\rm cir}$ grows with entropy scale k_s [due to an increasing thermal pressure, Fig. 4(e)] and when the equatorial angular velocity $\Omega_{\rm eq}$ approaches the Keplerian one $\Omega_{\rm kep}$ [since the configuration approach mass shedding, Fig. 4(f)]. Assuming that the configuration collapses to a black hole, one can estimate the mass of the accretion disk that remains outside of the innermost stable circular orbit (see discussion in Sec. III D). The disk mass $M_{\rm disk}$ also grows when the equatorial angular velocity approaches the Keplerian one, as expected. It is worth pointing out that, when present, the estimated mass of the accretion disk is of the order of that expected from simulations, e.g., Refs. [5,39,52,53], and much larger than the one that is expected from a single rotating NS [31,32].

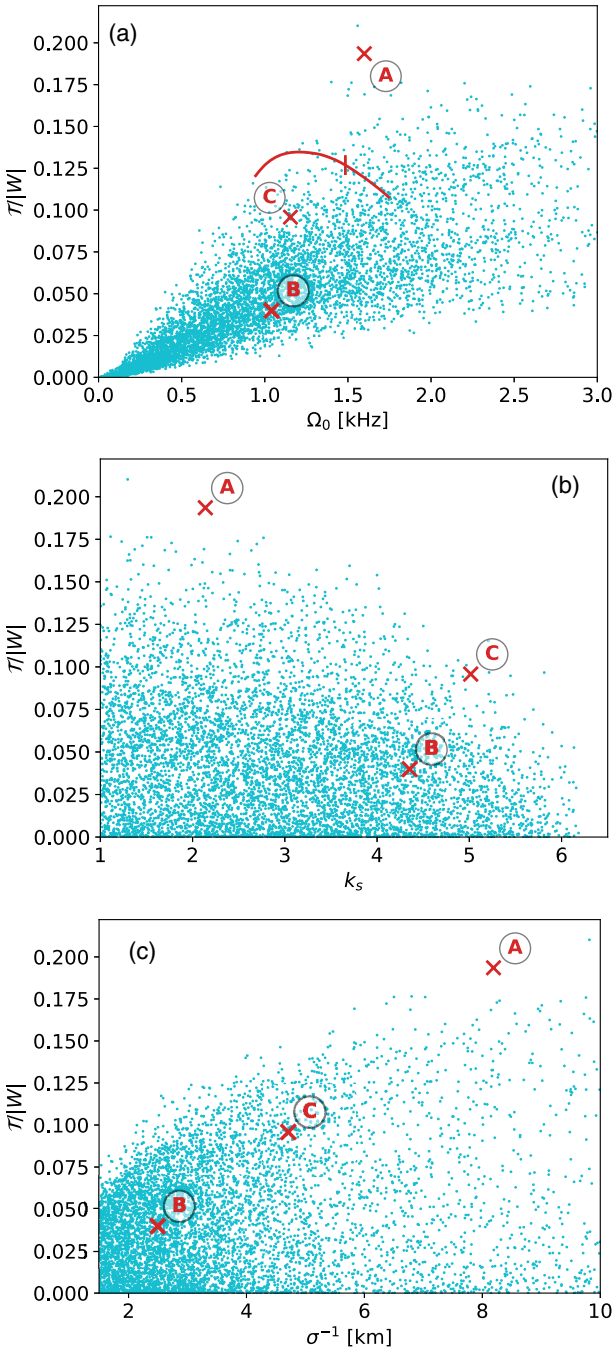

FIG. 5. Kinetic-to-gravitational binding energy ratio $\mathcal{T}/|W|$ of the BNS merger remnant with the ALF2 EOS. Plot conventions are as in Fig. 2. Ω_0 is the angular velocity on the rotational axis, k_s the entropy scale parameter, and σ^{-1} the rotation law scale.

C. Stability

The solutions that are found for a given EOS are not necessarily dynamically stable. There are many types of instabilities that may be present (for a review see e.g., [54]), and whether or not a particular one is relevant depends on how its associated timescale compares with the timescale of the viscous processes at work. In this paper, we will consider a noncomprehensive set of possible instabilities that may be present in the remnant.

Low $\mathcal{T}/|W|$-instability.—The dynamical study of differentially rotating configurations allowed the discovery of the so-called "low-$\mathcal{T}/|W|$ instability" [22,55,56]. The low-$\mathcal{T}/|W|$ instability sets in when an oscillation mode corotates with the matter in a point of the star. Since in a BNS merger remnant the angular velocity is not monotonic with the radius, it is possible for an oscillation mode to corotate with the matter in two points [22,23]. Performing the numerical evolution in general relativity of an initially cold remnant with a rotation law from Uryū *et al.* [18], Xie *et al.* [23] found that this instability is present for the relatively low value of $\mathcal{T}/|W| = 0.16$, where $\mathcal{T}$ is the kinetic energy (not to be confused with the temperature) and $W = M_p + \mathcal{T} - M$ is the gravitational binding energy (M_p is the proper mass). Similarly, making use of Newtonian gravity, assuming the Cowling approximation, and exploring a larger number of remnant configurations, Passamonti and Andersson [22] found that this instability may set in for $\mathcal{T}/|W| \gtrsim 0.02$ and as $\mathcal{T}/|W|$ grows it initially becomes more relevant until the mode stabilizes to a specific value of $\mathcal{T}/|W|$. We find that $\mathcal{T}/|W|$ grows for increasing axial angular velocity Ω_0 [Fig. 5(a)], and that the maximum of $\mathcal{T}/|W|$ decreases with increasing entropy scale k_s [Fig. 5(b)] and increasing rotational scale σ^{-1} [Fig. 5(c)]. The anticorrelation between $\mathcal{T}/|W|$ and k_s is not mediated through the central density ρ_0 since both Ω_0 and k_s increase with increasing ρ_0, cf. Figs. 2(a) and 2(b). We interpret the anticorrelation of k_s and $\mathcal{T}/|W|$ with the fact that, increasing the thermal pressure, the star is less strongly bound. We conclude that a larger entropy content contributes in stabilizing the star against the low-$\mathcal{T}/|W|$ instability.

Convective instability.—The convective instability has a local character and sets in when a displaced fluid element is accelerated away from its equilibrium position. In a hot, rotating star, the forces that are applied on a fluid element are gravity, buoyancy (due to the pressure gradient), and the centrifugal force, see e.g., [57].

In a nonrotating and hence spherical star, convective instability is driven by buoyancy. In this case, necessary conditions for convective instability are a nonbarotropic EOS and entropy (or composition) gradients. For nonrotating NSs, the onset of convective instability is controlled by the Schwarzschild criterion [58], that is, a star is convectively unstable when the Schwarzschild discriminant $\bar{S}(\bar{r})$ is negative,

$$\bar{S}(\bar{r}) = \frac{\mathrm{d}p}{\mathrm{d}\bar{r}} - c_s^2 \frac{\mathrm{d}\epsilon}{\mathrm{d}\bar{r}} < 0, \tag{12}$$

where $\bar{r}$ is the Schwarzschild radius and c_s^2 is the speed of sound. As pointed out by Camelio *et al.* [26], for our EOS this is identical to

$$[(\Gamma_{\rm th}-1)(1+a_i)\rho+\Gamma_i k_i(\Gamma_{\rm th}-\Gamma_i)\rho^{\Gamma_i}]\frac{{\rm d}s}{{\rm d}\bar{r}}<0, \quad (13)$$

or, equivalently (since in our case $\Gamma_{\rm th}<\Gamma_i$), a star is unstable against convection if

$$\mathrm{sgn}(\rho_c-\rho)\cdot\mathrm{sgn}\left(\frac{{\rm d}s}{{\rm d}\bar{r}}\right)<0, \quad (14)$$

where the critical density ρ_c happens to be the same critical density for the EOS inversion (see Appendix A 1; the value of ρ_c for each EOS is reported in Table II and marked with a vertical line in Fig. 3). In our case, since the thermal law for the effective barotropic case is such that ${\rm d}s/{\rm d}\rho>0$ [we set $\Gamma_T=2/3$ in Eq. (10)], Eq. (14) tells us that if the density decreases monotonically from the center outward, then the star is stable in the region with $\rho<\rho_c$ and unstable for $\rho>\rho_c$.

On the other hand, in isentropic stars the driver for convective instability is the centrifugal force. When the isentropic star is differentially rotating, a necessary criterion for convective stability is [54,59]

$$\frac{{\rm d}j^2(r,\pi/2)}{{\rm d}r}>0, \quad (15)$$

where the square of the specific (per unit mass) angular momentum $j=\hbar u_\phi/\rho$ is differentiated along the equatorial plane, $\theta=\pi/2$. As shown in the top panel of Fig. 7, this criterion is generally respected with our differential rotation law.

Having a configuration that is differentially rotating, nonisentropic, and baroclinic (namely non effectively barotropic) at the same time means that the simple criteria (12) and (15) are no more valid. This is due to the fact that not only the gravitational force is no more balanced by the buoyant force alone, but also to the fact that the three forces are not necessary parallel. However, due to the qualitative nature of our discussion, we will still make use of criteria (14) and (15) to allow for this simple remark on the remnant stability: that an increase of ρ_0 favors a buoyancy-driven convective instability, because configurations with $\rho_0>\rho_c$ (right of the dotted line in Fig. 3) are convectively unstable (at least in a part of the star), while configurations $\rho_0<\rho_c$ (left of the dotted line in Fig. 3) are convectively stable if the density decreases monotonically with the radius everywhere (and the entropy increases with the radius). Note that convective instability has been found 30–50 ms after merge in numerical simulations [60,61], and some of our models do have negative entropy gradients at intermediate radii. We remark moreover that this already approximate consideration is valid only for the simplified EOSs we are considering. In a more realistic EOS, the value of $\Gamma_{\rm th}$ may be density dependent and the simple nonrotating convective instability criterion we derived, see Eqs. (13) and (14), should be revised.

Axisymmetric secular stability.—Another type of instability is the "secular instability." It sets in when a configuration evolves to a similar one with lower energy (i.e., a stabler one) on a timescale longer than the hydrodynamical one. Here we are concerned with axisymmetric instabilities, which can be determined simply by studying the stationary (axisymmetric) configurations. In practice, a configuration defined by a set of parameters is stable if all configurations close in the parameter space with the same baryon mass M_0, angular momentum J, and total entropy S, have a greater gravitational mass M. For rigidly rotating, isentropic NSs, secular stability can be checked with the turning point criterion [25,27–29], that is, a star becomes secularly unstable when[6]

$$\left.\frac{\partial M}{\partial\rho_0}\right|_{J,S}=0, \quad (16)$$

where ρ_0 is the central density. In the case of a cold and nonrotating NS, secular instability implies and is implied by instability against dynamical perturbations [62], while in general, for a rigidly rotating and isentropic star, secular instability is a sufficient but not necessary condition for instability against dynamical perturbations, e.g., [30].

In the general case we are interested in, namely differentially rotating, nonisentropic, and baroclinic NSs, the turning point criterion [Eq. (16)] cannot be applied because the number of free parameters is greater than the number of conserved quantities (i.e., M_0, S, J [28]). As an exercise, we applied anyway criterion (16) for the ALF2 EOS (for which we can compute J and S) and showed the result in Fig. 3. We stress that this should be taken as an *indication* for stability, since we know that the turning point criterion *cannot* be applied to our case (see also footnote 6). In any case, we can draw a couple of simple conclusions from this exercise: (i) we cannot draw a clear stable/unstable line in the ρ_0-M diagram, since it is a two-dimensional projection of the six-dimensional parameter space, and (ii) the marginally stable, cold, nonrotating and the cold, rigidly rotating, Keplerian configurations are in the region of the ρ_0-M diagram where the transition from stability to instability for our model is expected.

Apart for the turning point criterion, one can try to determine the stability of a configuration directly from the definition (namely that M is a minimum for constant M_0, J, S). A problem of this approach is that two configurations close in the parameter space may not be connected by any dynamical evolution, and therefore it would not make sense to compare their gravitational mass. In the case of the ALF2

[6]We remark that Eq. (16) is not the only condition required by the turning point criterion; an additional condition on the second order variation of the quantities should be considered (see Refs. [27,29] for additional details). For simplicity, and because we do not advocate the use of the turning point criterion for our model, we will not consider this additional condition.

TABLE I. Parameters and stellar quantities of the models shown in Sec. III D. The EOS is ALF2. The quantities are central density ρ_0, axial angular velocity Ω_0, entropy scale k_s, angular velocity ratio Ω_M/Ω_0 and rotation law scale σ^{-1}, baroclinic parameter b, gravitational and baryon mass M and M_0, stellar angular momentum J, average entropy per baryon mass S/M_0, kinetic-to-gravitational energy ratio $T/|W|$, circumferential radius $R_{\rm cir}$, Keplerian angular velocity at the equator $\Omega_{\rm kep}$, angular velocity at the equator $\Omega_{\rm eq}$, expected disk mass $M_{\rm disk}$, maximum temperature $T_{\rm max}$.

Quantity	A	B	C
ρ_0 $[\rho_n]$	2.097	3.808	9.767
Ω_0 [kHz]	1.599	1.044	1.154
k_s	2.138	4.354	5.015
Ω_M/Ω_0	1.056	1.118	1.071
σ^{-1} [km]	8.189	2.497	4.714
b	−0.6136	-2.465×10^{-4}	−1.589
M $[M_\odot]$	2.63	2.50	3.60
M_0 $[M_\odot]$	2.86	2.76	3.84
J $[M_\odot^2]$	5.92	2.34	11.4
S/M_0 $[k_B/m_n]$	2.54	3.60	7.09
$\mathcal{T}/\lvert W\rvert$	0.194	0.0398	0.0958
$R_{\rm cir}$ [km]	25.9	30.2	158
$\Omega_{\rm kep}$ [kHz]	0.712	0.547	0.560
$\Omega_{\rm eq}$ [kHz]	0.536	0.193	0.458
$M_{\rm disk}$ $[M_\odot]$	0.00	0.00	0.372
$T_{\rm max}$ [MeV]	45.5	47.5	112

EOS, for which we can compute M_0 and S, we tried anyway to look at the variation of M with respect to the parameters, keeping M_0, J, S constant. Unfortunately, we were not able to draw clear conclusions from this analysis and further work is required.[7]

D. Selected models

In this section we show the stellar profiles for three selected models, chosen according to the following criteria:

(A) a model that is a plausible outcome of a BNS merger,
(B) the model with $M < 4$ that is closest to an effectively barotropic configuration, namely that with the baroclinic parameter b closest to zero, to be compared with model A,
(C) the model with the greatest disk mass and $M < 4$.

The specific model parameters and properties are summarized in Table I and their rest mass density, temperature, and angular velocity distribution are shown in Figs. 6–9.

Model A is a realistic BNS merger remnant. Its mass M, angular momentum J, and central density ρ_0 are in the expected range, e.g., [63,64]. Its shape is qualitatively similar to that obtained in simulations (cf. Fig. 13 in Perego *et al.* [4]). The temperature forms a hot ring in the equatorial plane (cf. Fig. 7 of Perego *et al.* [4]); the temperature profile is continuous but not smooth due to the fact that the EOS is piecewise defined. The angular velocity curve peaks 3–4 km from the rotational axis (cf. Fig. 5 of Hanauske *et al.* [5], where the peak is expected at 7–10 km).

Baroclinicity is fundamental in order to obtain the right thermal distribution. This can be realized comparing the profiles of models A and B (the latter being almost effectively barotropic): in model A the density and temperature isocontours are not parallel and this permits the existence of the hot equatorial ring, while in model B they are parallel and as a consequence the temperature profile has an onionlike shape. This is a consequence of baroclinicity [26].

Between the three chosen models, model C has the biggest circumferential radius and its equatorial angular velocity is the closest to the Keplerian one. Unsurprisingly, a significant amount of matter with large specific angular momentum is present. In case of black hole formation, this matter could form a disk. We followed the approach of Margalit *et al.* [31] (see also Shapiro *et al.* [65] and Camelio *et al.* [32]), namely we computed the baryon mass of the matter whose angular momentum per unit mass j is larger than that of the innermost stable circular orbit of a black hole with the same mass and angular momentum of the original system.[8] This is equivalent to assuming that there is no angular momentum transfer or loss during the collapse and that dynamical effects like shocks play no role, which is clearly not true, e.g., [33,34], but at the same time it is a first order approximation that allows us to make a semiquantitative estimation of the expected disk mass $M_{\rm disk}$. We found it to be $M_{\rm disk} \approx 0.4\ M_\odot$, which is substantially larger than that expected from the collapse of a marginally stable, Keplerian, rigidly rotating, cold NS [31,32]. The disk mass is in the range of what is expected from dynamical simulations (actually at the upper end of the expectations) [5,12,39,52,53,66,67]. With a large potential energy reservoir of $3.6\times10^{52}\ {\rm erg}(\epsilon/0.05)(M_{\rm disk}/0.4\ M_\odot)$, this configuration is a good candidate for launching a powerful short Gamma Ray Burst (GRB), provided that the energy can be deposited in a low enough density environment. For the latter, one

[7]It would be interesting, in the future, to find a physically motivated parametrization of the star with a number of free parameters less or equal to the number of global constraints on the stellar evolution (i.e., three), so that the turning point criterion [27,28] would be applicable, and to compare this secular stability with dynamical simulations as done by Takami *et al.* [30] and Camelio *et al.* [32].

[8]Note that this is not consistent, since when some matter escapes black hole formation, its mass and angular momentum should not contribute to the black hole total mass and angular momentum. However, local energy is not well defined in general relativity. We checked with the extreme case of model C that an iterative procedure [65] would result in a disk mass about 12% smaller than in our approach, which is an acceptable level of precision.

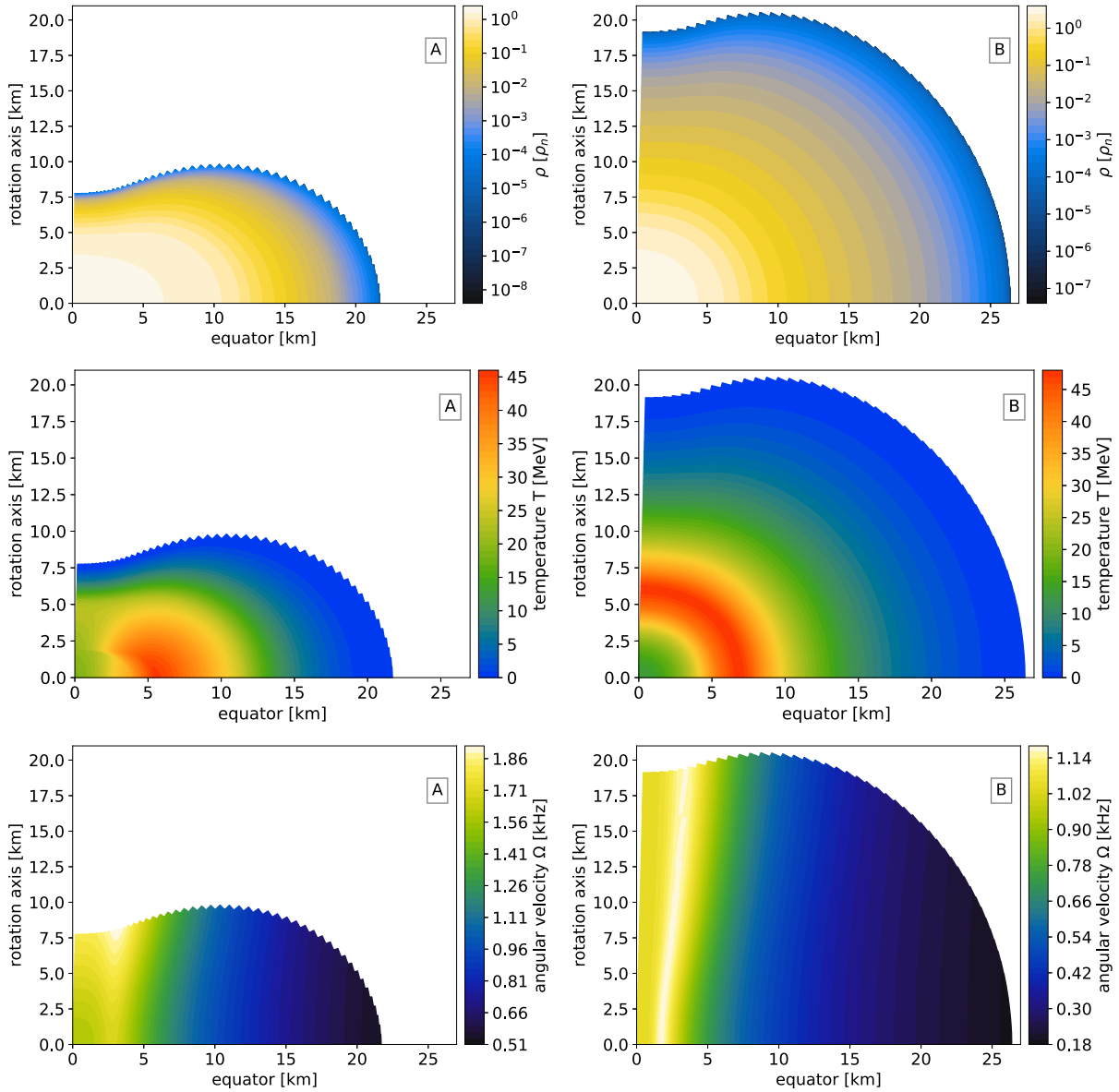

FIG. 6. Density ρ, temperature T, and angular velocity Ω profiles of models A and B.

usually assumes that the central object needs to collapse to a black hole, but see [68] for the possibility to launch relativistic outflows in the presence of a central neutron star.

In Fig. 8 we compare the profiles of $\Omega(r)$ along the equator for our models A, B, and C and that obtained by Hanauske *et al.* [5] from the merger of two $M = 1.25$ stars with the ALF2 EOS and a $\Gamma_{\rm th} = 1.8$ thermal component (Hanauske *et al.* [5] found that the rotational profile of the remnant is almost independent from the value of $\Gamma_{\rm th}$, see their Fig. 16). Our model reproduces the qualitative features of the simulated rotational profiles (e.g., the off-axis maximum of the angular velocity), but there are quantitative differences. In particular, the maximum of the angular velocity is much closer to the rotational axis in our models rather than in Hanauske *et al.* [5].

In Fig. 9 we show a histogram of the thermodynamical properties of the matter for models B and C, like those in Perego *et al.* [4]. First, we note the defining difference between the (almost) effectively barotropic configuration of model B and the baroclinic (i.e., nonbarotropic) configuration of model C: given a value of the density, there is only one value of temperature that can be obtained in model B, while this is not true for model C. Second, we remark that the models reproduce the qualitative features of the histograms in Perego *et al.* [4] (e.g., the polytropic increase of the temperature with the density, the maximum of the temperature reached off center, and the baroclinicity), but there are quantitative differences, most notably a smaller variation of the temperature for a given density in model C compared to the simulation results of Perego *et al.* [4].

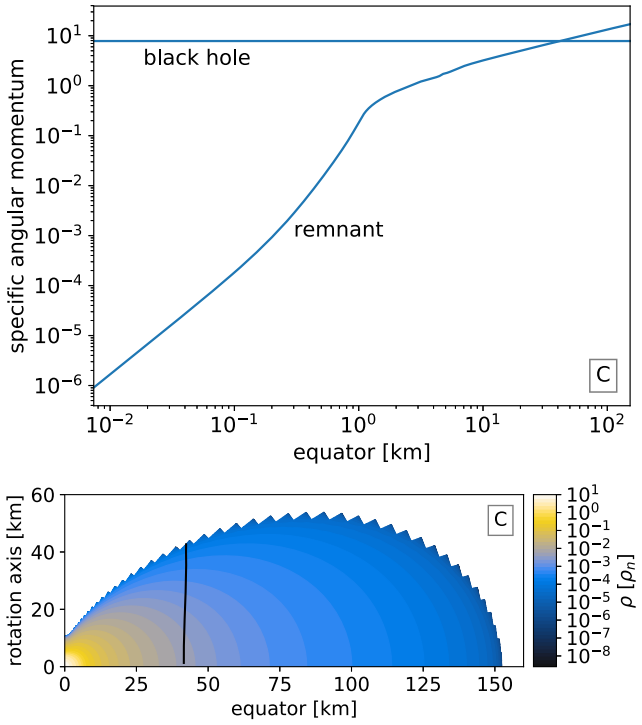

FIG. 7. Angular momentum per unit mass along the equator (j, top) and density profile (ρ, bottom) of model C. In the top panel, the horizontal line is the angular momentum per unit mass of the innermost stable circular orbit of the black hole with the same mass and angular momentum of model C. In the bottom panel, the black line separates the matter expected to fall onto the black hole in case of stellar collapse from that forming the accretion disk.

In future works, we will refine our model and the code in order to improve the quantitative comparison with the results of dynamical simulations.

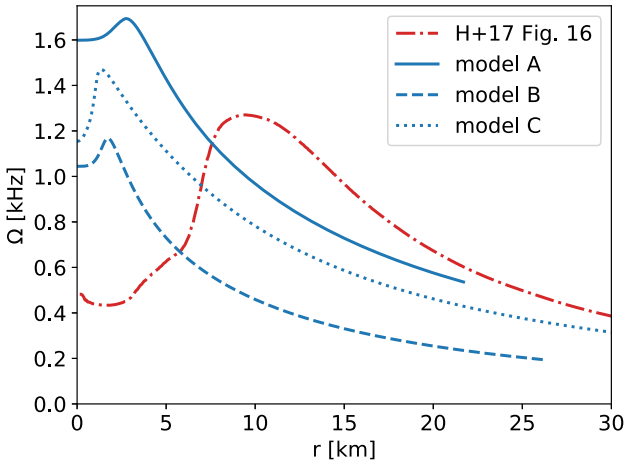

FIG. 8. Rotational profiles of models A (straight blue line), B (dashed blue line), and C (dotted blue line) and of the ALF2-M125 $\Gamma_{th} = 1.8$ model of Hanauske *et al.* (Fig. 16 of Ref. [5]) (dot-dashed red line).

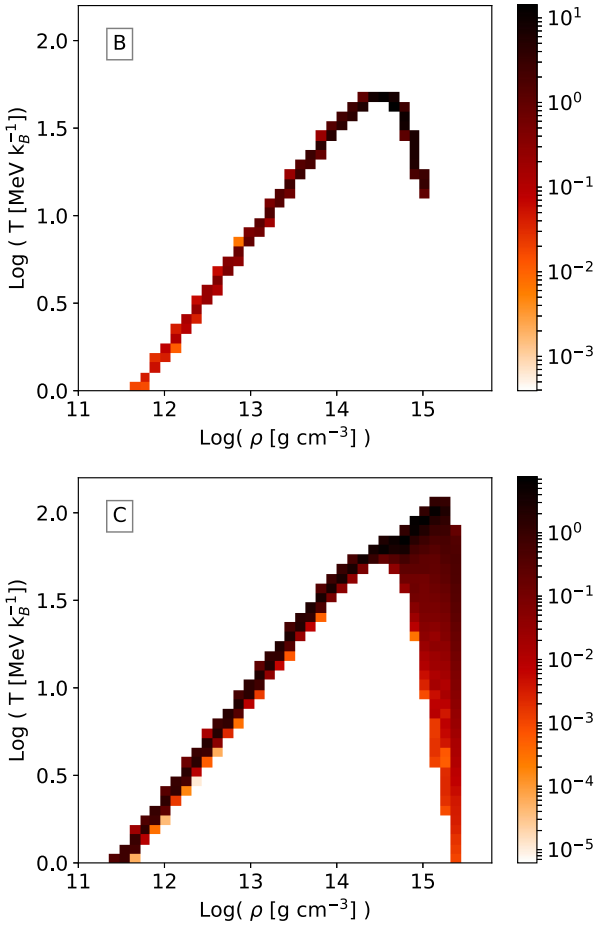

FIG. 9. Mass-weighted, normalized histogram of the thermodynamical distribution (temperature vs rest mass density) of matter for models B (top) and C (bottom), to be compared with Perego *et al.* [4].

We provide the community with ten realistic BNS remnant models (including model A) with the ALF2 EOS and stellar properties in the ranges $2.4 < M < 3.5$, $5.5 < J < 7.5$, $1.5 < \rho_0/\rho_n < 4$, $\Omega_M/\Omega_0 > 1.05$, compatible to numerical relativity simulations, e.g., [69,70], plus models B and C. The stellar profiles and a PYTHON script to read them can be downloaded from Zenodo [35]. This dataset can be used as background models for microphysical studies or as initial conditions for dynamical evolution.

IV. CONCLUSION

In this paper we studied realistic stationary models for postmerger configurations after a BNS merger. We modeled the EOS with cold polytropic pieces [36] plus a thermal component as described in more detail in [26]. Our remnant model is controlled by the central density and other parameters that fix the rotational and thermal distributions. We explored a broad range of postmerger configurations and discussed their stability based on qualitative criteria.

In particular we have

(i) introduced new rotation and thermal laws, Eqs. (8) and (10), that are motivated by numerical simulations [4,5].
(ii) applied the technique recently developed by Camelio *et al.* [26] to BNS merger remnants. We obtained baroclinic (i.e., not effectively barotropic) configurations, which are more suitable to model merger remnants than the effectively barotropic ones [4].
(iii) performed an extensive parameter space study in which we included the effects of differential rotation, temperature, and baroclinicity.

Our main results are

(i) the central density ρ_0, the axial angular velocity Ω_0, and the thermal scale k_s are the parameters that have the largest impact on the global remnant properties, see Fig. 4.
(ii) baroclinicity (implemented with the parameter b) is necessary to reproduce the thermodynamical profile of BNS merger remnants, in particular the existence of a hot ring in the equatorial plane [4,21], compare models A and B in Sec. III D.
(iii) the collapse of a BNS merger remnant to a black hole may generate a massive disk which could provide the central engine to launch a short gamma ray burst [31,32], see Figs. 4(d) and 7.
(iv) the increase of the central density ρ_0 may cause convective instabilities and the increase of the axial angular velocity Ω_0 may cause low-$\mathcal{T}/|W|$ instability. If no convection is present, an increased thermal content (k_s) seems to increase stability by reducing the maximal $\mathcal{T}/|W|$ that can be reached by the model.
(v) we make the results of our parameter search and a set of realistic models available to the community [35].

The approach described here can be extended further:

(i) an even more realistic description of the remnant physics, namely (a) the inclusion of composition in the model, (b) the adoption of more realistic EOSs (for example the new piecewise parametrization of O'Boyle *et al.* [71] or a tabulated EOS), (c) the addition of the magnetic field (see Ref. [72] for an example of protoneutron star studied in Newtonian gravity), and (d) the use of a rotation curve that is truly Keplerian by construction, not only because it approaches the Keplerian trend at large radii (like in this work and in Uryū *et al.* [18]), but also the Keplerian frequency.
(ii) addition of physically motivated restrictions on the free parameters of the stationary remnant model to simplify the study of its stability and the test of these predictions with dynamical simulations [5,32] and/or a perturbative study [73,74].

In this way it will be possible to perform realistic fits of the mergers remnant obtained by dynamical simulations.

ACKNOWLEDGMENTS

We are grateful to Marco Antonelli, Lorenzo Gavassino, Albino Perego, and Matthias Hanauske for useful discussions. We also thank Panagiotis Iosif and Nikolaos Stergioulas for comments on an early draft of this work and for sharing with us a manuscript on a related topic. We are grateful to the authors of Hanauske *et al.* [5] for providing the data shown in Fig. 8. G. C. and B. H. acknowledge support from the National Science Center Poland (NCN) via OPUS Grant No. 2019/33/B/ST9/00942. S. R. has been supported by the Swedish Research Council (VR) under Grant No. 2016-03657_3, by the Swedish National Space Board under Grant No. Dnr. 107/16, the research environment grant Gravitational Radiation and Electromagnetic Astrophysical Transients (GREAT) funded by the Swedish Research council (VR) under Dnr 2016-06012 and by the Knut and Alice Wallenberg Foundation under Dnr 2019.0112. We acknowledge stimulating interactions with the COST Actions CA16104 "Gravitational waves, black holes and fundamental physics" (GWverse) and CA16214 "The multimessenger physics and astrophysics of neutron stars" (PHAROS). The authors gratefully acknowledge the Italian Istituto Nazionale di Fisica Nucleare (INFN), the French Centre National de la Recherche Scientifique (CNRS) and the Netherlands Organization for Scientific Research, for the construction and operation of the Virgo detector and the creation and support of the EGO consortium. B. H. acknowledges support from the National Science Center Poland (NCN) via SONATA BIS Grant No. 2015/18/E/ST9/00577.

APPENDIX A: IMPLEMENTATION DETAILS

1. Equation of state

We adopt a set of EOSs obtained with different methods and different components: ALF2 (nuclear-quark hybrid

TABLE II. EOS properties. For each EOS, we report the EOS high-density polytropic index Γ_7; the EOS thermal constant $k_{\rm th}$; the temperature $T_{2,2} = T(2\rho_n, 2\ {\rm k_B})$; the critical density for the EOS inversion ρ_c; the central density $\rho_{\rm tov}$ of the maximal mass $M_{\rm tov}$ nonrotating configuration; the circumferential radius $R_{1.4}$ of the nonrotating configuration with $M = 1.4$; the maximum stellar angular momentum J^r_M, maximum angular rotation Ω^r_M, and maximal mass M^r_M on the stable branch of the Keplerian curve of a rigidly rotating and cold NS.

Quantity	ALF2	SLy	APR4	ENG
Γ_7	1.890	2.851	3.348	3.168
$k_{\rm th}$	1.993	1.215	0.9610	1.385
$T_{2,2}$ [MeV]	37.9	23.1	18.3	26.3
ρ_c [ρ_n]	45.0	5.58	4.44	4.35
$\rho_{\rm tov}$ [ρ_n]	6.11	7.49	7.14	6.65
$M_{\rm tov}$ [$M_\odot$]	1.98	2.05	2.19	2.24
$R_{1.4}$ [km]	12.5	11.6	11.2	11.8
J^r_M [$M^2_\odot$]	4.07	4.03	4.83	5.03
Ω^r_M [kHz]	1.48	1.85	1.98	1.85
M^r_M [$M_\odot$]	2.43	2.43	2.61	2.68

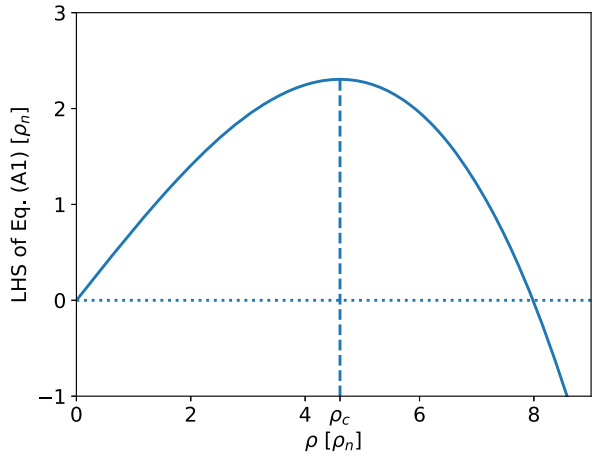

FIG. 10. Left-hand side of Eq. (A1) for the $\Gamma = 3$ EOS of Camelio *et al.* [26]. ρ_c is the critical density for the inversion.

EOS [40]), SLy (nuclear EOS from an effective potential [41]), APR4 (nuclear EOS from variational method [42]), and ENG (relativistic Brueckner-Hartree-Fock nuclear EOS [43]). We use the parametrization of Read *et al.* [36] to implement them, including the SLy crust (we use only one index $i = 1, \ldots, 7$ running from the crust to high density). We summarize the EOS properties in Table II.

In order to recover ρ, s from $\mathscr{h}$, p, we note that Eq. (B14) of [26] can be generalized to

$$(\Gamma_{\rm th} - 1)(1 + a_i)\rho + (\Gamma_{\rm th} - \Gamma_i)k_i\rho^{\Gamma_i} = (\Gamma_{\rm th} - 1)\mathscr{h} - \Gamma_{\rm th}p. \tag{A1}$$

Given a couple of $\mathscr{h}$, p we can get 0, 1, or more different couples of ρ, s, see Fig. 10. It is important to know if the couple $\mathscr{h}$, s admits at least one solution, because otherwise such couple is not valid and the algorithm should be able to mark that point as "vacuum outside the surface." On the other hand, whether or not the solution of the EOS is unique is somehow less important because the only quantities that enter in the Einstein and Euler equations for an ideal gas are $\mathscr{h}$ and p and not ρ and s. This means that one can find a valid stellar configuration without knowing the rest mass and entropy distributions inside the star.

In the case of a piecewise polytropic EOS such as Eq. (1), the degeneracy can in principle be more problematic than for a one-piece polytropic one because there can be more than 2 valid ρ, s couples for given $\mathscr{h}$, p. An analysis of the piecewise EOSs considered in this paper shows that this is not the case: the degeneracy is the same of the one-piece polytropic EOS of Camelio *et al.* [26], i.e., there is only one critical density ρ_c in the range of the last high-density piece,[9] $\rho_c > \rho_6$. In Table II we report the critical density for each EOS considered; apart for the ALF2 EOS, for which $\rho_c \simeq 45\rho_n$, the other critical densities lie in the range $4\rho_n \lesssim \rho_c \lesssim 6\rho_n$ and are even lower than the central density of the maximal mass configuration of the spherical (nonrotating) model. Since the ALF2 has such a high value of ρ_c, we can safely choose the low density branch of the solution like we did in Camelio *et al.* [26], while we cannot do the same for the other EOSs. For this reason, we are able to compute the total stellar rest mass M_0, entropy S, and disk mass $M_{\rm disk}$ only for ALF2. All other quantities, such the stellar gravitational mass M and angular momentum J, can be computed also for the other EOSs.

2. Neutron star

We used a modified version [26,32] of the XNSv2 code [44,45]; we refer the reader to the original papers for details on the implementation. The only difference with respect to our previous work [26] is that, at the beginning of the iterative procedure to determine the stellar configuration, we have slowly increased the thermal and rotational content of the star by varying k_s and Ω_0, in order to increase the stability of the numerical scheme. We set the following parameters in our code:

(i) inner radial grid: boundary at $r = 30\ M_\odot$, 3000 evenly spaced points,
(ii) outer radial grid: boundary at $1000\ M_\odot$, 3000 increasingly spaced points,
(iii) absolute tolerance of $\max(\mathscr{h})$ for convergence: 10^{-11},
(iv) planar symmetry,
(v) 50 points in the angular grid (in one of the hemispheres),
(vi) 500 relaxing iterations (see discussion above),
(vii) 30 Legendre polynomials.

In order to implement the rotation law (8), we define two functions G_1 and G_2:

[9] In practice we studied Eq. (A1) in the range of each polytropic piece and checked whether the critical density $\rho_{c,i}$, given by cf. Eq. (B15) of [26],

$$\rho_{c,i}^{\Gamma_i - 1} = -\frac{(\Gamma_{\rm th} - 1)(1 + a_i)}{(\Gamma_{\rm th} - \Gamma_i)k_i\Gamma_i}, \tag{A2}$$

(i) exists (i.e., the rhs is positive) and (ii) lays in the correct range (i.e., $\rho_{i-1} \le \rho_{c,i} \le \rho_i$). We found that, for the EOSs considered, the only piece with a critical density [respecting conditions (i)–(ii)] is the last one, and we therefore write $\rho_c \equiv \rho_{c,7}$. Note that if the rhs of Eq. (A1) is negative and ρ_c exists the only valid solution is the high-density one with $\rho > \sqrt[\Gamma_7 - 1]{\Gamma_7}\rho_c$. On the other hand, it can be that $\rho_c < \rho < \sqrt[\Gamma_7 - 1]{\Gamma_7}\rho_c$ [i.e., the rhs of Eq. (A1) is positive], but the recovered s^2 is negative, that is the entropy is not physical and the only valid solution is the low-density one. Unfortunately, in general one cannot exclude one specific branch.

$$G_1(F) = \bar{G}(F)\Theta(F_0 - F) + G(F)\Theta(F - F_0), \quad \text{(A3)}$$

$$G_2(F) = G(F)\Theta(F_0 - F) + \bar{G}(F)\Theta(F - F_0), \quad \text{(A4)}$$

where Θ is the step function and

$$\bar{G}(F) = G_0 - \frac{\Omega_0 + \Omega_M}{2} F_0 - \Omega_M (F - F_0) - (F - F_0)^3. \quad \text{(A5)}$$

We start by solving the system (3) and (4) with $G \equiv G_1$. If $F < F_0$, then we solve again the system with $G \equiv G_2$. We found that in this way we increase the precision of the solution close to the maximum, $F \simeq F_0$. Moreover, instead of solving the Newton-Raphson with F as an independent variable, we found that it is numerically more stable to solve the equations using Ω as an independent variable, even if the rotation law is defined in F.

The heat function [Eq. (7)] is determined by numerical integration.

[1] J. M. Lattimer, The nuclear equation of state and neutron star masses, Annu. Rev. Nucl. Part. Sci. **62**, 485 (2012).

[2] O. Benhar and S. Fantoni, *Nuclear Matter Theory* (CRC Press, Boca Raton, 2020), https://www.taylorfrancis.com/books/nuclear-matter-theory-omar-benhar-stefano-fantoni/10.1201/9781351175340.

[3] B. P. Abbott *et al.*, GW170817: Observation of Gravitational Waves from a Binary Neutron Star Inspiral, Phys. Rev. Lett. **119**, 161101 (2017).

[4] A. Perego, S. Bernuzzi, and D. Radice, Thermodynamics conditions of matter in neutron star mergers, Eur. Phys. J. A **55**, 124 (2019).

[5] M. Hanauske, K. Takami, L. Bovard, L. Rezzolla, J. A. Font, F. Galeazzi, and H. Stöcker, Rotational properties of hypermassive neutron stars from binary mergers, Phys. Rev. D **96**, 043004 (2017).

[6] B. P. Abbott *et al.*, Multi-messenger observations of a binary neutron star merger, Astrophys. J. Lett. **848**, L12 (2017).

[7] A. Bauswein and H.-Th. Janka, Measuring Neutron-Star Properties via Gravitational Waves from Binary Mergers, Phys. Rev. Lett. **108**, 011101 (2012).

[8] A. Bauswein, N. Stergioulas, and H.-T. Janka, Revealing the high-density equation of state through binary neutron star mergers, Phys. Rev. D **90**, 023002 (2014).

[9] K. Takami, L. Rezzolla, and L. Baiotti, Constraining the Equation of State of Neutron Stars from Binary Mergers, Phys. Rev. Lett. **113**, 091104 (2014).

[10] K. Takami, L. Rezzolla, and L. Baiotti, Spectral properties of the postmerger gravitational-wave signal from binary neutron stars, Phys. Rev. D **91**, 064001 (2015).

[11] S. Bernuzzi, T. Dietrich, and A. Nagar, Modeling the Complete Gravitational Wave Spectrum of Neutron Star Mergers, Phys. Rev. Lett. **115**, 091101 (2015).

[12] S. Bernuzzi, Neutron star merger remnants, General Relativity and Gravitation **52**, 108 (2020).

[13] M.-R. Wu, I. Tamborra, O. Just, and H.-T. Janka, Imprints of neutrino-pair flavor conversions on nucleosynthesis in ejecta from neutron-star merger remnants, Phys. Rev. D **96**, 123015 (2017).

[14] S. Abbar and H. Duan, Fast neutrino flavor conversion: Roles of dense matter and spectrum crossing, Phys. Rev. D **98**, 043014 (2018).

[15] I. Tamborra and S. Shalgar, New developments in flavor evolution of a dense neutrino gas, arXiv:2011.01948.

[16] I. Hachisu, A versatile method for obtaining structures of rapidly rotating stars, Astrophys. J. Suppl. Ser. **61**, 479 (1986).

[17] H. Komatsu, Y. Eriguchi, and I. Hachisu, Rapidly rotating general relativistic stars. I—Numerical method and its application to uniformly rotating polytropes, Mon. Not. R. Astron. Soc. **237**, 355 (1989).

[18] K. Uryū, A. Tsokaros, L. Baiotti, F. Galeazzi, K. Taniguchi, and S. Yoshida, Modeling differential rotations of compact stars in equilibriums, Phys. Rev. D **96**, 103011 (2017).

[19] M. Shibata, K. Taniguchi, and K. Uryū, Merger of binary neutron stars with realistic equations of state in full general relativity, Phys. Rev. D **71**, 084021 (2005).

[20] W. Kastaun and F. Galeazzi, Properties of hypermassive neutron stars formed in mergers of spinning binaries, Phys. Rev. D **91**, 064027 (2015).

[21] W. Kastaun, R. Ciolfi, and B. Giacomazzo, Structure of stable binary neutron star merger remnants: A case study, Phys. Rev. D **94**, 044060 (2016).

[22] A. Passamonti and N. Andersson, Merger-inspired rotation laws and the low-T/W instability in neutron stars, Mon. Not. R. Astron. Soc. **498**, 5904 (2020).

[23] X. Xie, I. Hawke, A. Passamonti, and N. Andersson, Instabilities in neutron-star postmerger remnants, Phys. Rev. D **102**, 044040 (2020).

[24] P. Iosif and N. Stergioulas, Equilibrium sequences of differentially rotating stars with post-merger-like rotational profiles, Mon. Not. R. Astron. Soc. stab392 (2021).

[25] J. O. Goussard, P. Haensel, and J. L. Zdunik, Rapid uniform rotation of protoneutron stars, Astron. Astrophys. **321**, 822 (1997), http://aa.springer.de/bibs/7321003/2300822/small.htm.

[26] G. Camelio, T. Dietrich, M. Marques, and S. Rosswog, Rotating neutron stars with nonbarotropic thermal profile, Phys. Rev. D **100**, 123001 (2019).

[27] R. Sorkin, A criterion for the onset of instability at a turning point, Astrophys. J. **249**, 254 (1981).

[28] R. D. Sorkin, A stability criterion for many parameter equilibrium families, Astrophys. J. **257**, 847 (1982).

[29] J. L. Friedman, J. R. Ipser, and R. D. Sorkin, Turning point method for axisymmetric stability of rotating relativistic stars, Astrophys. J. **325**, 722 (1988).

[30] K. Takami, L. Rezzolla, and S. Yoshida, A quasi-radial stability criterion for rotating relativistic stars, Mon. Not. R. Astron. Soc. **416**, L1 (2011).
[31] B. Margalit, B. D. Metzger, and A. M. Beloborodov, Does the Collapse of a Supramassive Neutron Star Leave a Debris Disk? Phys. Rev. Lett. **115**, 171101 (2015).
[32] G. Camelio, T. Dietrich, and S. Rosswog, Disc formation in the collapse of supramassive neutron stars, Mon. Not. R. Astron. Soc. **480**, 5272 (2018).
[33] V. Ravi and P. D. Lasky, The birth of black holes: Neutron star collapse times, gamma-ray bursts and fast radio bursts, Mon. Not. R. Astron. Soc. **441**, 2433 (2014).
[34] P. D. Lasky, B. Haskell, V. Ravi, E. J. Howell, and D. M. Coward, Nuclear equation of state from observations of short gamma-ray burst remnants, Phys. Rev. D **89**, 047302 (2014).
[35] G. Camelio, T. Dietrich, S. Rosswog, and B. Haskell, Axisymmetric models for neutron star merger remnants with realistic thermal and rotational profiles: Dataset (2020), https://zenodo.org/record/4268501#.YDztpIZ7n0o.
[36] J. S. Read, B. D. Lackey, B. J. Owen, and J. L. Friedman, Constraints on a phenomenologically parametrized neutron-star equation of state, Phys. Rev. D **79**, 124032 (2009).
[37] A. Bauswein, H. T. Janka, and R. Oechslin, Testing approximations of thermal effects in neutron star merger simulations, Phys. Rev. D **82**, 084043 (2010).
[38] H. Yasin, S. Schäfer, A. Arcones, and A. Schwenk, Equation of State Effects in Core-Collapse Supernovae, Phys. Rev. Lett. **124**, 092701 (2020).
[39] T. Dietrich, M. W. Coughlin, P. T. H. Pang, M. Bulla, J. Heinzel, L. Issa, I. Tews, and S. Antier, Multimessenger constraints on the neutron-star equation of state and the Hubble constant, Science **370**, 1450 (2020).
[40] M. Alford, M. Braby, M. Paris, and S. Reddy, Hybrid stars that masquerade as neutron stars, Astrophys. J. **629**, 969 (2005).
[41] F. Douchin and P. Haensel, A unified equation of state of dense matter and neutron star structure, Astron. Astrophys. **380**, 151 (2001).
[42] A. Akmal, V. R. Pandharipande, and D. G. Ravenhall, Equation of state of nucleon matter and neutron star structure, Phys. Rev. C **58**, 1804 (1998).
[43] L. Engvik, E. Osnes, M. Hjorth-Jensen, G. Bao, and E. Ostgaard, Asymmetric nuclear matter and neutron star properties, Astrophys. J. **469**, 794 (1996).
[44] N. Bucciantini and L. Del Zanna, General relativistic magnetohydrodynamics in axisymmetric dynamical spacetimes: The X-ECHO code, Astron. Astrophys. **528**, A101 (2011).
[45] A. G. Pili, N. Bucciantini, and L. Del Zanna, Axisymmetric equilibrium models for magnetized neutron stars in general relativity under the conformally flat condition, Mon. Not. R. Astron. Soc. **439**, 3541 (2014).
[46] J. A. Isenberg, Waveless approximation theories of gravity, Int. J. Mod. Phys. D **17**, 265 (2008).
[47] I. Cordero-Carrión, P. Cerdá-Durán, H. Dimmelmeier, J. L. Jaramillo, J. Novak, and E. Gourgoulhon, Improved constrained scheme for the Einstein equations: An approach to the uniqueness issue, Phys. Rev. D **79**, 024017 (2009).
[48] P. Iosif and N. Stergioulas, On the accuracy of the IWM-CFC approximation in differentially rotating relativistic stars, Gen. Relativ. Gravit. **46**, 1800 (2014).
[49] M. A. Abramowicz, The relativistic von Zeipel's theorem, Acta Astron. **21**, 81 (1971), https://ui.adsabs.harvard.edu/abs/1971AcA....21...81A/abstract.
[50] G. Camelio, L. Gualtieri, J. A. Pons, and V. Ferrari, Spin evolution of a proto-neutron star, Phys. Rev. D **94**, 024008 (2016).
[51] B. Haskell, J. L. Zdunik, M. Fortin, M. Bejger, R. Wijnands, and A. Patruno, Fundamental physics and the absence of sub-millisecond pulsars, Astron. Astrophys. **620**, A69 (2018).
[52] D. Radice, A. Perego, K. Hotokezaka, S. A. Fromm, S. Bernuzzi, and L. F. Roberts, Binary neutron star mergers: Mass ejection, electromagnetic counterparts and nucleosynthesis, Astrophys. J. **869**, 130 (2018).
[53] M. W. Coughlin, T. Dietrich, B. Margalit, and B. D. Metzger, Multimessenger Bayesian parameter inference of a binary neutron star merger, Mon. Not. R. Astron. Soc. **489**, L91 (2019).
[54] J. L. Friedman and N. Stergioulas, Stability of relativistic stars, Bull. Astron. Soc. India **39**, 21 (2011), https://ui.adsabs.harvard.edu/abs/2011BASI...39...21F/abstract.
[55] J. M. Centrella, K. C. B. New, L. L. Lowe, and J. D. Brown, Dynamical rotational instability at low T/W, Astrophys. J. Lett. **550**, L193 (2001).
[56] A. L. Watts, N. Andersson, and D. I. Jones, The nature of low $T/|W|$ dynamical instabilities in differentially rotating stars, Astrophys. J. Lett. **618**, L37 (2005).
[57] M. A. Abramowicz, Rayleigh and Solberg criteria reversal near black holes: The optical geometry explanation, arXiv:astro-ph/0411718.
[58] K. S. Thorne, Validity in general relativity of the Schwarzschild criterion for convection, Astrophys. J. **144**, 201 (1966).
[59] J. M. Bardeen, A variational principle for rotating stars in general relativity, Astrophys. J. **162**, 71 (1970).
[60] R. De Pietri, A. Feo, J. A. Font, F. Löffler, F. Maione, M. Pasquali, and N. Stergioulas, Convective Excitation of Inertial Modes in Binary Neutron Star Mergers, Phys. Rev. Lett. **120**, 221101 (2018).
[61] R. De Pietri, A. Feo, J. A. Font, F. Löffler, M. Pasquali, and N. Stergioulas, Numerical-relativity simulations of long-lived remnants of binary neutron star mergers, Phys. Rev. D **101**, 064052 (2020).
[62] C. W. Misner and H. S. Zapolsky, High-Density Behavior and Dynamical Stability of Neutron Star Models, Phys. Rev. Lett. **12**, 635 (1964).
[63] T. M. Tauris *et al.*, Formation of double neutron star systems, Astrophys. J. **846**, 170 (2017).
[64] B. P. Abbott *et al.*, GW190425: Observation of a compact binary coalescence with total mass $\sim 3.4\ M_{\odot}$, Astrophys. J. Lett. **892**, L3 (2020).
[65] S. L. Shapiro, Collapse of uniformly rotating stars to black holes and the formation of disks, Astrophys. J. **610**, 913 (2004).
[66] V. Nedora, F. Schianchi, S. Bernuzzi, D. Radice, B. Daszuta, A. Endrizzi, A. Perego, A. Prakash, and F. Zappa, Mapping dynamical ejecta and disk masses from numerical relativity simulations of neutron star mergers, arXiv:2011.11110.

[67] V. Nedora, S. Bernuzzi, D. Radice, B. Daszuta, A. Endrizzi, A. Perego, A. Prakash, M. Safarzadeh, F. Schianchi, and D. Logoteta, Numerical relativity simulations of the neutron star merger GW170817: Long-term remnant evolutions, winds, remnant disks, and nucleosynthesis, Astrophys. J. **906**, 98 (2021).

[68] P. Mösta, D. Radice, R. Haas, E. Schnetter, and S. Bernuzzi, A magnetar engine for short GRBs and kilonovae, Astrophys. J. Lett. **901**, L37 (2020).

[69] T. Dietrich, D. Radice, S. Bernuzzi, F. Zappa, A. Perego, B. Brügmann, S. V. Chaurasia, R. Dudi, W. Tichy, and M. Ujevic, CoRe database of binary neutron star merger waveforms, Classical Quantum Gravity **35**, 24LT01 (2018).

[70] K. Kiuchi, K. Kawaguchi, K. Kyutoku, Y. Sekiguchi, and M. Shibata, Sub-radian-accuracy gravitational waves from coalescing binary neutron stars in numerical relativity. II. Systematic study on the equation of state, binary mass, and mass ratio, Phys. Rev. D **101**, 084006 (2020).

[71] M. F. O'Boyle, C. Markakis, N. Stergioulas, and J. S. Read, Parametrized equation of state for neutron star matter with continuous sound speed, Phys. Rev. D **102**, 083027 (2020).

[72] S. K. Lander, P. Haensel, B. Haskell, J. L. Zdunik, and M. Fortin, Magnetic fields in late-stage proto-neutron stars, Mon. Not. R. Astron. Soc. stab460 (2021).

[73] C. J. Krüger and K. D. Kokkotas, Fast Rotating Relativistic Stars: Spectra and Stability without Approximation, Phys. Rev. Lett. **125**, 111106 (2020).

[74] C. J. Krüger and K. D. Kokkotas, Dynamics of fast rotating neutron stars: An approach in the Hilbert gauge, Phys. Rev. D **102**, 064026 (2020).